CHEMISTRY OF MATERIALS
Article

Chem. Mater. **2009,** *21,* 3853–3864 3853
DOI:10.1021/cm901644e

Structures, Phase Transitions, Hydration, and Ionic Conductivity of $Ba_4Nb_2O_9$

Chris D Ling,*[,†,‡] Maxim Avdeev,[‡] Ramzi Kutteh,[‡,§] Vladislav V Kharton,[⊥] Aleksey A Yaremchenko,[⊥] Svitlana Fialkova,[⊥,||] Neeraj Sharma,[†] René B Macquart,[†,‡] Markus Hoelzel,[¶] and Matthias Gutmann[#]

[†]*School of Chemistry, The University of Sydney, Sydney 2006, Australia;,* [‡]*Bragg Institute, ANSTO, PMB 1, Menai 2234, Australia,* [§]*School of Physics, The University of Sydney, Sydney 2006, Australia,* [⊥]*Department of Ceramics and Glass Engineering, CICECO, University of Aveiro, 3810-193 Aveiro, Portugal,* [||]*North Carolina A&T State University, Fort IRC Building, Suite 242, Greensboro, North Carolina 27411,* [¶]*Technischen Universität München, FRM II, Lichtenbergstrasse 1, 85747 Garching, Germany, and* [#]*ISIS, Science and Technology Facilities Council, Rutherford Appleton Laboratory, Didcot OX11 0QX, United Kingdom.*

Received June 14, 2009. Revised Manuscript Received July 22, 2009

$Ba_4Nb_2O_9$ is shown to have two basic polymorphs: a high-temperature γ phase, which represents an entirely new structure type; and a low-temperature α phase, which has the rare $Sr_4Ru_2O_9$ structure type. The phases are separated by a reconstructive phase transition at ~1370 K, the kinetics of which are sufficiently slow that the γ phase can easily be quenched to room temperature. Below ~950 K, both α and γ phases absorb significant amounts of water. In the case of the γ phase, protons from absorbed water occupy ordered positions in the structure, giving rise to a stoichiometric phase γ-III-$Ba_4Nb_2O_9 \cdot 1/3H_2O$ at room temperature. γ-III-$Ba_4Nb_2O_9 \cdot 1/3H_2O$ partially dehydrates at ~760 K to give another stoichiometric phase γ-II-$Ba_4Nb_2O_9 \cdot 1/6H_2O$, which completely dehydrates at ~950 K to γ-I-$Ba_4Nb_2O_9$. The hydrated γ phases exhibit faster protonic and oxide ionic transport than the hydrated α phases because of the presence in the gamma phases of 2D layers containing Nb^{5+} cations with unusually low oxygen coordination numbers (4 or 5) separated by discrete OH groups. Hydration appears to play an important role in stabilizing the γ phases at low temperatures, with the $\gamma \rightarrow \alpha$ transition on reheating a quenched sample occurring at higher temperatures in humid atmospheres.

Introduction

Proton-conducting materials have important potential applications including fuel cells membranes and electrodes, batteries, and sensors. A number of oxides exhibit significant proton conductivity, and although polymers such as Nafion and acid salts such as $CsHSO_4$ show higher conductivities at room temperature, these oxides remain of interest because they are far more stable at the higher operating temperatures advantageous for fuel cells and steam electrolyzers (typically 500−1000 K).[1,2] The rare earth-doped $BaCeO_3$ oxides are the most promising proton-conducting oxides so far, with the highest reported conductivities,[3] but unfortunately they are chemically unstable in wet or CO_2-containing atmospheres. It is therefore of interest to discover and characterize new candidates.

In this context, recent reports of significant proton conductivity in $LaNbO_4$,[4−6] $Ba_3Ca_{1+x}Nb_{2-x}O_{9-3x/2}$[7−9] (known as BCN18 at its optimal composition $x = 0.18$) and $HLaNb_2O_7 \cdot 0.5H_2O$[10] have led to renewed interest in the structural and physical properties of niobium oxides. This report concerns $Ba_4Nb_2O_9$,[11−14] which clearly has a close chemical relationship to $Ba_3Ca_{1+x}Nb_{2-x}O_{9-3x/2}$ at $x = 0$. However, the structures − and therefore the possible ionic conduction mechanisms − of the two compounds are very different. $Ba_3Ca_{1+x}Nb_{2-x}O_{9-3x/2}$ is a 1:2 ordered perovskite built of exclusively corner-connected CaO_6 and NbO_6 octahedra, in which long-range-disordered oxygen vacancies are introduced by overdoping Ca^{2+} for Nb^{5+}.

*Corresponding author. E-mail: c.ling@chem.usyd.edu.au.

(1) Kreuer, K. D. *Annu. Rev. Mater. Res.* **2003**, *33*, 333–359.
(2) Norby, T. *Solid State Ionics* **1999**, *125*(1−4), 1–11.
(3) Zuo, C. D.; Zha, S. W.; Liu, M. L.; Hatano, M.; Uchiyama, M. *Adv. Mater.* **2006**, *18*(24), 3318–+.
(4) Haugsrud, R.; Norby, T. *J. Am. Ceram. Soc.* **2007**, *90*(4), 1116–1121.
(5) Haugsrud, R.; Norby, T. *Solid State Ionics* **2006**, *177*(13−14), 1129–1135.
(6) Haugsrud, R.; Norby, T. *Nat. Mater.* **2006**, *5*(3), 193–196.
(7) Du, Y.; Nowick, A. S. *Solid State Ionics* **1996**, *91*(1−2), 85–91.
(8) Nowick, A. S.; Du, Y. *Solid State Ionics* **1995**, *77*, 137–146.
(9) Liang, K. C.; Du, Y.; Nowick, A. S. *Solid State Ionics* **1994**, *69*(2), 117–120.
(10) Kobayashi, Y.; Schottenfeld, J. A.; Macdonald, D. D.; Mallouk, T. E. *J. Phys. Chem. C* **2007**, *111*(7), 3185–3191.
(11) Bezjak, J.; Jancar, B.; Recnik, A.; Suvorov, D. *J. Eur. Ceram. Soc.* **2008**, *28*(14), 2771–2776.
(12) Blasse, G. *J. Inorg. Nucl. Chem.* **1965**, *27*(5), 993–1003.
(13) Leshchenko, P. P.; Lykova, L. N.; Kovba, L. M.; Stefanovich, S. Y.; Chechkin, V. V. *Inorg. Mater.* **1985**, *21*(2), 227–230.
(14) Leshchenko, P. P.; Paromova, M. V.; Lykova, L. N.; Kovba, L. M. *Vest. Mosk. Univ., Ser. 2: Khim.* **1979**, *20*(2), 148–151.

Published on Web 08/05/2009

These oxygen vacancies allow fast migration of oxide anions and protons when hydrated. In contrast, although the structure(s) of $Ba_4Nb_2O_9$ had not been solved prior to this study, it has always been clear from X-ray diffraction (XRD) patterns that it is not a 1:2 ordered perovskite; and an analogous overdoping scheme of Ba^{2+} for Nb^{5+} to produce oxygen vacancies is extremely unlikely, given the huge size difference between these cations (effective ionic radii of 1.35 and 0.64 Å in 6-fold coordination respectively[15]), nor is it observed experimentally. As $Ba_4Nb_2O_9$ was reported to show a reconstructive phase transition at ~1400 K,[13,14] which should facilitate ionic conduction, we decided to investigate conductivity and hydration in $Ba_4Nb_2O_9$ in parallel with an attempt to solve the structures of the various phases. This was fortuitous, as the complex structural behavior of this compound turns out to be intimately linked with its hydration behavior.

$Ba_4Nb_2O_9$ is an ostensibly simple solid-state compound that has proved remarkably difficult to characterize. It was first synthesized in 1965 by Blasse,[12] who reported that its structure was complex, but probably a distorted variant of 6H-type hexagonal perovskite ($BaTiO_3$-type). The only other significant reports in the literature were by Leschenko et al.[13,14] in 1979 and then 1985, who used differential thermal analysis (DTA), optical spectroscopy and fixed-frequency AC dielectric measurements to reveal an extremely complex sequence of structural phase transitions. Identifying the transition temperatures allowed them to isolate individual phases by quenching from high temperatures, which they studied by XRD. They proposed unit cells and approximate space group symmetries, but the complexity of these cells—up to 6300 $Å^3$ in orthorhombic space groups—put structure solution well-beyond the reach of contemporary XRD instrumentation.

The key observations of Leschenko et al.[13,14] were that the highest temperature phase (γ-$Ba_4Nb_2O_9$) was only thermodynamically stable above 1400 K, below which it transformed slowly (over several hours) to α-$Ba_4Nb_2O_9$; and that γ-$Ba_4Nb_2O_9$ could therefore be easily quenched to room temperature. This suggests that the $\gamma \rightarrow \alpha$ phase transition involves a reconstruction of the cation array. On heating quenched metastable γ-$Ba_4Nb_2O_9$ from room temperature, they reported a series of relatively fast and reversible phase transitions at 520 and 780 K (to phases they labeled β and β' respectively) before a slow (presumably reconstructive) transition to thermodynamically stable α-$Ba_4Nb_2O_9$ above 970 K.

Bezjak et al.[11] recently reinvestigated the phase transitions of $Ba_4Nb_2O_9$ using XRD and microwave dielectric measurements. They did not solve any of the structures of $Ba_4Nb_2O_9$ but confirmed the majority of the findings of Leschenko et al.,[13,14] and clarified the close structural relationship between the quenched high-temperature γ phase and the β phase obtained on subsequent heating to ~550 K. They reported that further heating above 830 K resulted in the slow-cooled α phase.

Finally, it should also be noted Wu et al. also recently reported the dielectric properties of nanocrystalline $Ba_4Nb_2O_9$ synthesized by a hydrothermal route under very basic conditions (pH ≥ 14).[16] They Rietveld-refined the crystal structure in cubic $Fm\bar{3}m$ space group symmetry as a partially disordered rock-salt-type 1:1 double perovskite. However, the published structure and XRD pattern do not match any polymorphs reported by Leschenko et al.[13,14] or Bezjak et al.[11] (or obtained in the present study), indicating that this phase is not stable under standard (less basic) conditions.

In this article, we report a detailed investigation into the structure and physicochemical properties—in particular, the electronic and ionic conductivity—of the various forms of $Ba_4Nb_2O_9$ obtained under standard conditions.

Experimental Methods

Single-phase polycrystalline samples of $Ba_4Nb_2O_9$ were prepared by solid-state synthesis in air from $BaCO_3$ and Nb_2O_5 (99.99% purity or greater). Prior to weighing, $BaCO_3$ was dried at 1000 K overnight and Nb_2O_5 was annealed in air at 1370 K for 2 h. The stoichiometric mixture was ground in an agate mortar and pestle, calcined at 1300 K for 20 h with several regrindings and then ball-milled. Following the method of Leschenko et al.,[13,14] approximately half of this sample (~10 g) was heated to 1420 K for 20 h in an alumina crucible, removed from the furnace and quenched on a steel plate to produce the high-temperature γ-$Ba_4Nb_2O_9$ phase, whereas the other half of the sample was heated to 1320 K for 20 h and allowed to cool slowly in a muffle furnace to produce the low-temperature α-$Ba_4Nb_2O_9$ phase.

Dense ceramics of α-$Ba_4Nb_2O_9$ were prepared for ionic conductivity measurements and dilatometry by pressing disk- and bar-shaped samples uniaxially at 250–300 MPa and sintering them at 1870 K for 10 h in air. Finally, after polishing, the samples were annealed in air at 1320 K for 50 h. The density of the α-$Ba_4Nb_2O_9$ pellets was found to be 5.28 g cm^{-3}, or 93% of the theoretical density based on the structural model presented in this paper. Ceramic samples of the quenched high-temperature γ-$Ba_4Nb_2O_9$ phase could only be prepared by sintering of the green compacts below 1200 K (to avoid the transition back to α-$Ba_4Nb_2O_9$), because of cracking of the pellets upon quenching from above 1400 K. The density of these ceramics was found to be only 4.2 g cm^{-3} or ~75%.

Single crystals of the high-temperature form of $Ba_4Nb_2O_9$ were grown in a Crystal Systems Corporation FZ-T-10000-H-VI-VPM-PC optical floating-zone furnace with 300 W filaments. Crystals were grown from a polycrystalline feed rod of γ-$Ba_4Nb_2O_9$ that was pressed at 60 MPa in a hydrostatic press, then sintered at 1420 K for 1 h in a vertical tube furnace.

Room-temperature XRD data were collected on a Shimadzu XRD-6000 using Cu K_α radiation. High-temperature synchrotron XRD (S-XRD) data were collected at the Powder Diffraction Beamline of the Australian Synchrotron at $\lambda = 0.82563$ Å; samples were placed in unsealed 1 mm diameter quartz capillaries and heated with a hot air blower to 1270 K over 12 h, with data collected at 20 K intervals.

(15) Brese, N. E.; O'Keeffe, M. *Acta Crystallogr., Sect. B* **1991**, *47*, 192–197.

(16) Wu, S. Y.; Chen, X. M.; Liu, X. Q. *J. Alloys Compd.* **2008**, *453*(1–2), 463–469.

Room-temperature neutron powder diffraction (NPD) data were collected on the instrument Echidna at the OPAL reactor (Lucas Heights, Australia) at $\lambda = 1.621$ Å; samples were placed in 9 mm diameter vanadium cans and data collected over 4 h per sample. High-temperature NPD data were collected on the instrument SPODI at the FRM-II research reactor (Garching, Germany) at $\lambda = 1.5482$ Å; samples were placed in 8 mm diameter sealed vanadium cans and heated up to 1470 K with a cylindrical niobium element, while complete data sets were collected over 1−6 h each at selected temperatures.

Single-crystal X-ray diffraction data were collected from a small (<0.1 mm diameter) crystal at room temperature on a Bruker-Nonius FR591 Kappa Apex II, using Mo-K_α (λ = 0.71073 Å) radiation from a rotating anode generator. Single-crystal neutron diffraction data were collected from a large (~100 mm^3) crystal at room temperature on the instrument SXD at ISIS (Rutherford Appleton Laboratories, UK).

Structural parameters were refined by geometry optimization using the VASP density functional theory code,[17,18] with symmetry switched off, and at the Γ point only in reciprocal space, because of the large size of the supercell (1536 atoms). Ionic relaxation was performed with the conjugate-gradient algorithm by varying atomic positions, keeping cell volume and shape fixed. The residual minimization method with direct inversion in the iterative subspace (RMM-DIIS) was used for the electronic relaxation with energy cutoff of 300 eV. The electron−electron interactions were described within the generalized-gradient approximation (GGA) using the Perdew-Burke-Ernzerhof (PBE) exchange-correlation functional.[19] The Ba, Nb, O, and H atoms were treated in the $5s^2 5p^6 6s^2$, $4p^6 4d^4 5s^1$, $2s^2 2p^4$, and $1s^1$ valence states, respectively, and interactions between ionic cores and valence electrons were described with the standard VASP projector-augmented wave (PAW) potentials.

Differential thermal analysis (DTA) data were collected on a Setaram LabSys TG-DTA16 instrument (heating rate 2 K min^{-1}) in air. Thermogravimetric analysis (TGA) data were collected on a Setaram SetSys 16/18 instrument (heating/cooling rate 2 K min^{-1}; sensitivity 0.4 μg; initial sample weight 0.7−0.9 g) in air.

Total (ionic + electronic) conductivity, σ, was determined by AC impedance spectroscopy (HP4284A precision LCR meter, 20 Hz−1 MHz) and a four-probe DC technique in air, argon or 10%H_2-90%N_2 mixture flows. The gas flows were dried by passing through silica gel or humidified by bubbling through water. The water vapor partial pressures in the dry and wet gases measured by a Jumo humidity transducer at room temperature were ~5 Pa and 2.8 kPa, respectively. The criterion for equilibration after a change in either atmosphere or temperature included the relaxation of the sample resistance less than 0.5% during 30 min. The equilibration time after each change in the external conditions varied in the range 3 to 80 h, increasing in the vicinity of phase boundaries discussed below. Ion transference numbers were evaluated by measurements of the electromotive force (EMF) of the concentration cells using the dry O_2/ambient air and wet O_2/ambient air gradients.[20−22] The measurements were performed at 973−1223 K using dense α-$Ba_4Nb_2O_9$ disks; attempts to test γ-$Ba_4Nb_2O_9$ failed because of the excessive porosity of the ceramics and non-negligible penetration of the potential-determining species. For all electrical measurements, the oxygen partial pressure in the gas flows was continuously monitored using yttria-stabilized zirconia (YSZ) sensors.

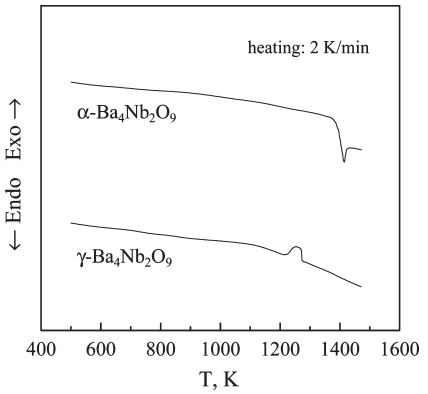

Figure 1. DTA curves of as-prepared powdered $Ba_4Nb_2O_9$ on heating in ambient air ($p(H_2O) \approx 1.2$ kPa). For α-$Ba_4Nb_2O_9$, the endothermic effect at 1370 ± 10 K is associated with the α → γ reconstructive phase transition. For γ-$Ba_4Nb_2O_9$, the exothermic effect at 1210 ± 10 K shows the transition of metastable quenched phase into thermodynamically stable α-$Ba_4Nb_2O_9$.

Results and Discussion

1. Temperature-Dependent Phase Transitions. XRD of our polycrystalline samples confirmed that γ-$Ba_4Nb_2O_9$ can be easily quenched from above 1400 K and converted back to α-$Ba_4Nb_2O_9$ on reheating close to this temperature, whereas α-$Ba_4Nb_2O_9$ is obtained by annealing below 1400 K. DTA was used to more precisely locate the γ → α transitions at 1370 ± 10 K on cooling the stable form and 1210 ± 10 K on warming the metastable quenched form (this is significantly different to the 970 K γ → α transition reported by Leschenko et al.,[13,14] but in agreement with the results of Bezjak et al.[11]) (Figure 1).

The structural phase transitions on heating quenched γ-$Ba_4Nb_2O_9$ were investigated in an in situ high-temperature S-XRD experiment. These data show transitions at approximately the same temperatures as reported by Leschenko et al. for β → β′ (780 K) and β′ → α (970 K).[13,14] However, they clearly show that the last of these transitions is not to α-$Ba_4Nb_2O_9$, but to another form related to γ-$Ba_4Nb_2O_9$, in agreement with our DTA data and the report of Bezjak et al.[11] that places the transition to α-$Ba_4Nb_2O_9$ at 1210 ± 10 K (Figure 1). The strongest peaks in all these diffraction patterns could be indexed to an orthorhombic unit cell $a \approx 6.1$ Å, $b \approx 12.5$ Å, $c \approx 10.6$ Å, which is clearly related by $a/2$, $b/2$, $c/2$ to the γ-$Ba_4Nb_2O_9$ cell of Leschenko et al. (a = 12.03 Å, b = 20.99 Å, c = 24.81 Å).[13,14] However, our data also reveal that the low-temperature phase below 760 K is distorted to monoclinic ($\beta \approx 90.3°$).

Part of the S-XRD patterns is shown in Figure 2. Below ~760 K, the unit cell is monoclinic and no superstructure peaks are observed. Note, however, that superstructure peaks were clearly observed for this phase in single crystal data−see below. Between ~760 and ~950 K, the unit cell

(17) Kresse, G.; Furthmuller, J. *Phys. Rev. B* **1996**, *54*(16), 11169–11186.
(18) Kresse, G.; Joubert, D. *Phys. Rev. B* **1999**, *59*(3), 1758–1775.
(19) Perdew, J. P.; Burke, K.; Ernzerhof, M. *Phys. Rev. Lett.* **1996**, *77* (18), 3865–3868.
(20) Goel, A.; Tulyaganov, D. U.; Kharton, V. V.; Yaremchenko, A. A.; Agathopoulos, S.; Ferreira, J. M. F. *J. Am. Ceram. Soc.* **2007**, *90*(7), 2236–2244.
(21) Kharton, V. V.; Marozau, I. P.; Mather, G. C.; Naumovich, E. N.; Frade, J. R. *Electrochim. Acta* **2006**, *51*(28), 6389–6399.
(22) Kharton, V. V.; Marques, F. M. B.; Tsipis, E. V.; Viskup, A. P.; Vyshatko, N. P.; Patrakeev, M. V.; Naumovich, E. N.; Frade, J. R. *Solid State Ionics* **2004**, *168*(1−2), 137–151.

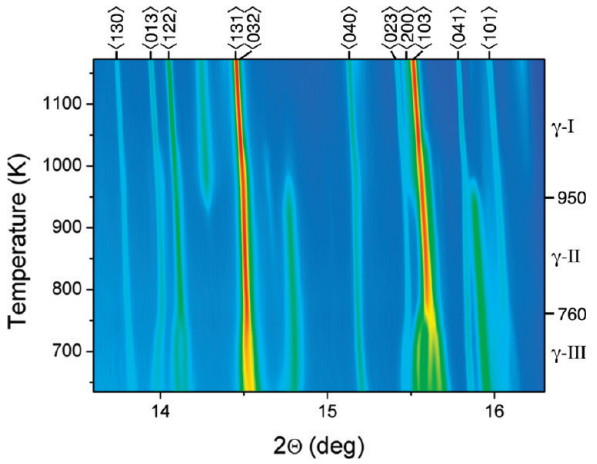

Figure 2. Part of the S-XRD (λ = 0. 82563 Å) patterns of quenched γ-$Ba_4Nb_2O_9$ collected on heating, showing a series of phase transitions. Indexing of peaks corresponds to the orthorhombic $a \approx 6.1$, $b \approx 12.5$, $c \approx 10.6$ Å subcell. Note the monoclinic splitting in the γ-III regime, and the different satellite peaks (unindexed) in the γ-II versus γ-I regimes.

is orthorhombic and superstructure peaks are observed corresponding to (at least) $2a$, $2b$, $2c$; i.e., the γ-$Ba_4Nb_2O_9$ cell of Leschenko et al.[13,14] Above ~950 K, the unit cell is orthorhombic and a different set of superstructure peaks are observed. Some further weak transient satellites observed at ~950 K ($2\theta \approx 14.7°$) may represent a further (unstable) intermediate phase. Having established close structural and chemical relationships among the γ, β, and β' phases of Leschenko et al.,[13,14] and discovered an additional transition, we now propose a modified nomenclature whereby the γ-$Ba_4Nb_2O_9$-related phases are labeled γ-I ($T > 950$ K), γ-II ($760 < T < 950$ K), and γ-III ($T < 760$ K). (We designate the highest-temperature phase as γ-I because its structure should be closest to that of the stable high-temperature γ form above 1370 K.)

Structural transitions were also investigated in an in situ high-temperature NPD experiment on SPODI. NPD has certain advantages over XRD in this context: neutrons can easily penetrate the thick walls of a furnace required to homogeneously heat a sample to above 1400 K, allowing us to study the γ-I ↔ α transitions; and neutron diffraction is far more sensitive to oxygen atoms in the presence of heavy metals such as Ba and Nb. Data were collected while slowly heating a quenched sample of γ-III-$Ba_4Nb_2O_9$ from room temperature through the transitions to γ-II and γ-I, followed by the reconstructive phase transition to α-$Ba_4Nb_2O_9$ above 1200 K and back to γ-I-$Ba_4Nb_2O_9$ above 1400 K.

The evolution of the (subcell) lattice parameters and volume from 600−1000 K (obtained by Le Bail fits to S-XRD data) for the quenched sample is shown in Figure 3. Both transitions (γ-III → γ-II at ~760 K and γ-II → γ-I at ~950 K) are marked by contractions of the unit cell relative to the prevailing thermal expansion.

2. Hydration Behavior. In light of the recent observations of proton conduction in niobates, a possible explanation for the unit cell contractions would be that the low-temperature forms incorporate significant amounts of water, which is liberated on heating. TGA data confirmed

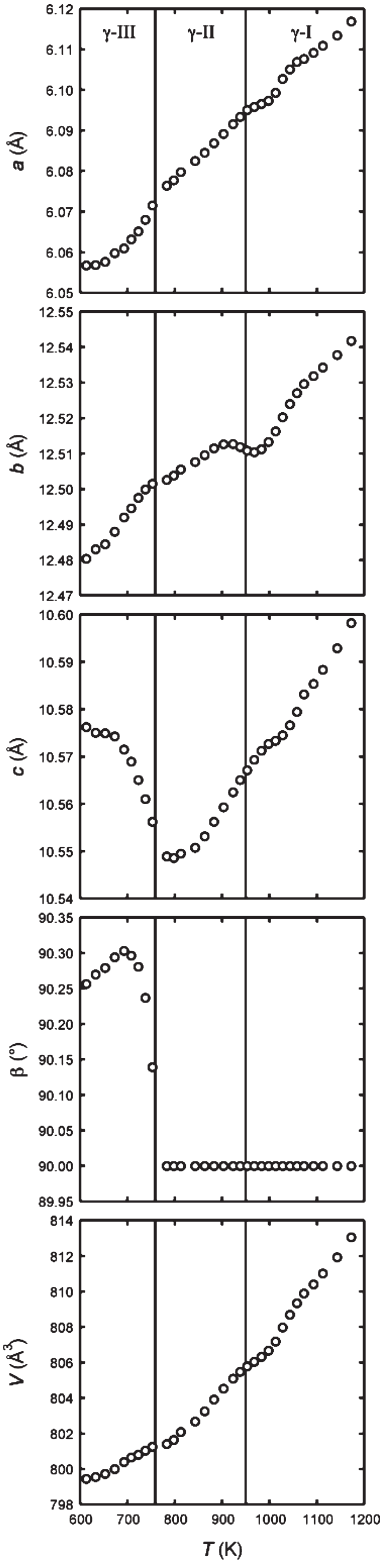

Figure 3. Evolution of the subcell lattice parameters of quenched γ-$Ba_4Nb_2O_9$ on heating, as determined by Le Bail fits to S-XRD data.

the existence of a stable hydrated phase at room temperature with a composition close to $Ba_4Nb_2O_9 \cdot 1/3H_2O$ (Figure 4). Furthermore, the TGA data indicated partial dehydration to another relatively stable phase with a composition close to $Ba_4Nb_2O_9 \cdot 1/6H_2O$ starting at ~750 K, followed by complete dehydration starting at ~1000 K. These dehydration steps correspond well to

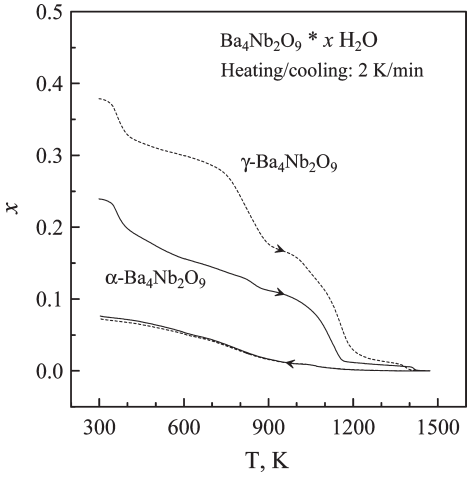

Figure 4. Variations of the water content in powdered $Ba_4Nb_2O_9$ samples on heating and then cooling in air at $p(H_2O) \approx 50$ Pa, as calculated from TGA data assuming that the samples contain no water at 1470 K and are oxygen-stoichiometric. (Note that additional water uptake at low temperatures is typical for oxide proton-conductors because of surface decomposition and water incorporation at grain boundaries.)

the γ-III → γ-II and γ-II → γ-I transitions respectively. The TGA data also show that the slow-cooled α-$Ba_4Nb_2O_9$ phase is hydrated at room temperature; at temperatures above 370 K the composition becomes close to $Ba_4Nb_2O_9 \cdot 1/6H_2O$. This phase dehydrates on heating over approximately the same temperature range as the quenched sample.

3. Structure Solution and Refinement. Understanding this complex and unusual hydration behavior clearly required solving the structures of $Ba_4Nb_2O_9$. NPD data at 1270 and 1470 K were used in our first attempts to determine the unit cells, space-group symmetries and crystal structures of α-$Ba_4Nb_2O_9$ and γ-I-$Ba_4Nb_2O_9$ respectively. The unit cell of α-$Ba_4Nb_2O_9$ was found to be $\sqrt{3}a$, $2b$ relative to the hexagonal cell proposed by Leschenko et al.[13,14] After exhaustive comparisons with known structures in chemically related systems, we determined that α-$Ba_4Nb_2O_9$ adopts the $Sr_4Ru_2O_9$-type structure[23] at 1270 K. This is a partially disordered structure consisting of Nb_2O_9 face-sharing octahedral dimers, which are aligned with the c axis and separated by voids almost as large as the dimers themselves. The structure is partially disordered because there are four possible positions for these dimers along the c axis, but only three crystallographically distinct sites. Figure 5 shows a short-range ordered version for clarity. The final Rietveld-refined fit to SPODI data using the GSAS software package[24] with the EXPGUI front-end[25] is shown in Figure 6, with refinement data and structural details summarized in Table 1. Some small deficiencies in the Rietveld fit may be indicative of partial ordering of the frustrated columns of Nb_2O_9 dimers, although no long-range-ordered model could be found that

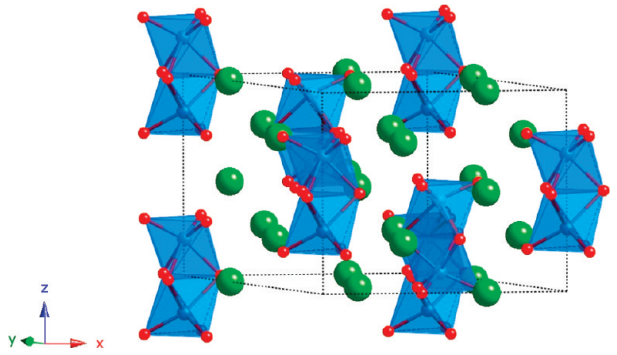

Figure 5. Structure of α-$Ba_4Nb_2O_9$ at 1270 K (showing a short-range ordered version of the partially disordered $Sr_4Ru_2O_9$-type structure for clarity), Rietveld-refined against NPD data. Ba atoms are drawn as green spheres; Nb_2O_9 dimers are shown as blue polyhedra with Nb atoms as blue spheres and O atoms as red spheres. Note the large voids between Nb_2O_9 dimers.

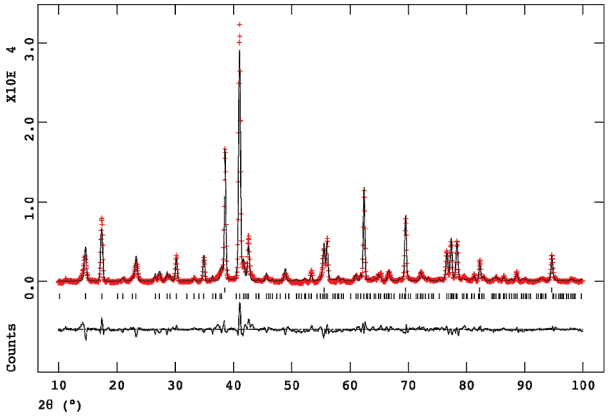

Figure 6. Observed (crosses), calculated (solid line),, and difference (below) NPD (SPODI, λ = 1.5482 Å) profiles for the final Rietveld-refinement of α-$Ba_4Nb_2O_9$ at 1270 K. The upper row of reflection markers indicate peaks due to the niobium heating elements.

Table 1. Structural Details for α-$Ba_4Nb_2O_9$ at 1270 K, Rietveld-Refined against NPD data (SPODI, λ = 1.5482 Å)[a]

atom	x (a)	y (b)	z (c)	$100U_{iso}$ (Å^3)
Ba1	0.668(3)	0	0	4.5(2)^1
Ba2	0.336(3)	0.0086(12)	1/4	4.5(2)^1
Nb1	0	0	0.155(3)	6.2(3)^2
Nb2	2/3	1/3	0.4378(13)	6.2(3)^2
O1	0.6751(17)	0.4956(14)	0.5210(9)	6.05(16)^3
O2	0.516(2)	0.347(2)	1/4	6.05(16)^3
O3	0.997(2)	0.839(2)	0.775(3)	6.05(16)^3
O4	0.148(3)	0	0	6.05(16)^3

[a] Space group hexagonal $P\bar{6}2c$ (No. 190); a = 10.3829(6) Å, c = 8.5722(8) Å. Goodness of fit = 4.44 for 36 refined parameters. Overall powder R factors: R_p = 0.0689, wR_p = 0.0897, $R(F^2)$ = 16.01. Superscript symbols indicate constraints.

significantly improved the fit. Full structural details including bond lengths are included in the deposited CIF file.

The structure of γ-I-$Ba_4Nb_2O_9$ at 1470 K was found to obey orthorhombic $Pmn2_1$ space group symmetry. No additional superstructure peaks were observed. Initial attempts to solve the structure were unsuccessful. A particular obstacle was posed by the volume of the unit cell, which strongly implies that the unit cell contains Z = 3 formula units of stoichiometric $Ba_4Nb_2O_9$; this made it

(23) Dussarrat, C.; Fompeyrine, J.; Darriet, J. *Eur. J. Solid State Inorg. Chem.* **1995**, *32*(1), 3–14.
(24) Larson, A. C.; von Dreele, R. B. *GSAS: The General Structure Analysis Program*; Los Alamos National Laboratory: Los Alamos, NM, 1990.
(25) Toby, B. H. *J. Appl. Crystallogr.* **2001**, *34*, 210–213.

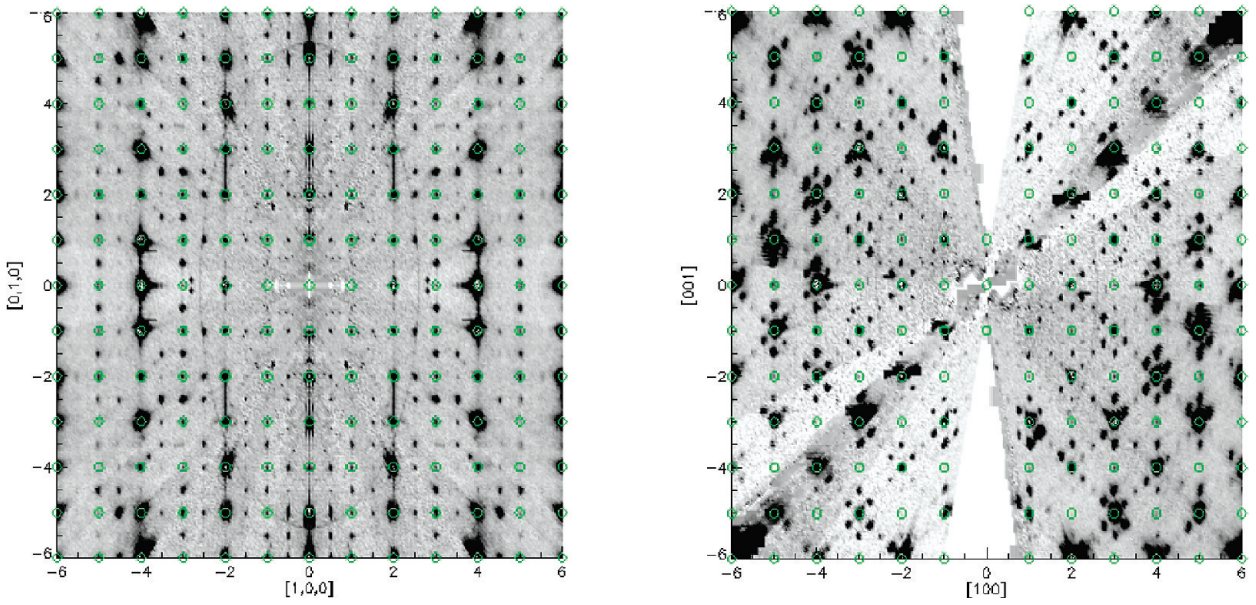

Figure 7. Reconstructed precession images from single-crystal neutron (SXD) data of quenched γ-$Ba_4Nb_2O_9$ at room temperature, clearly showing the $4 \times 2 \times 4$ supercell of the orthorhombic $Pmn2_1$ subcell. Subcell reflections are indexed and circled in green.

impossible to construct a chemically reasonable, fully ordered, model in $Pmn2_1$.

To improve our chances of solving the structures of the γ phases, we grew single crystals by the floating-zone furnace (FZF) method. Because the FZF effectively quenches a boule as it emerges from the molten hot zone, we expected to obtain γ-III-$Ba_4Nb_2O_9$ rather than α-$Ba_4Nb_2O_9$. Indeed, single crystals of γ-III-$Ba_4Nb_2O_9$ with volumes of up to 100 mm^3 were obtained from the grown boule.

Single-crystal X-ray diffraction data revealed an even larger supercell than reported by Leschenko et al.[13,14] for quenched γ-$Ba_4Nb_2O_9$: 4*a*, 2*b*, 4*c* relative to our $a \approx 6.1$ Å, $b \approx 12.5$ Å, $c \sim 10.6$ Å subcell. The only observed extinction condition in this supercell corresponds to a *B*-centering symmetry element. Figure 7 shows precession images reconstructed from single-crystal neutron diffraction data collected on SXD, with this supercell clearly visible, demonstrating that this ordering extends over very large domains. Unfortunately, however, the supercell was so large that peak overlap made it impossible to obtain reliable integrated intensities from SXD data.

The extremely high degree of pseudosymmetry that is necessarily present in such a large commensurate supercell led to the comprehensive failure of conventional "direct methods" approaches to structure solution from single-crystal X-ray diffraction data. We therefore used only the subcell reflections for preliminary structure solution, and retained the orthorhombic $Pmn2_1$ sym metry. Structure solution and refinement was carried out using the Jana2006 software package.[26] Direct methods were used to locate the first heavy metal atoms, followed by difference Fourier maps in conjunction with iterative least-squares structure refinements to locate oxygen atoms until the composition reached $Ba_6Nb_3O_{13}$ ($Z = 2$), which is slightly oxygen-deficient relative to the expected formula $Ba_6Nb_3O_{13.5}$ when $Z = 2$. The structure at this stage consisted of layers with isolated face-sharing Nb_2O_9 octahedral dimers, and layers with isolated NbO_4 tetrahedra. The final oxygen atom position was easily located in the Fourier difference map, but this peak was initially rejected as spurious because an isolated oxygen atom in this position would be extremely underbonded. Furthermore, tentative refinements indicated that this site would be fully occupied by oxygen, leading to the oxygen-excess charge-unbalanced composition $Ba_6Nb_3O_{14}$ ($Z = 2$). Both problems with the crystal chemistry of the structure at this stage could be resolved by the presence of a proton covalently bonded to this final oxygen site, giving an overall composition $Ba_6Nb_3O_{14}H$, $Z = 2$, which could alternatively be written $Ba_4Nb_2O_9 \cdot 1/3H_2O$, $Z = 3$, in agreement with the TGA results. However, because X-ray diffraction is relatively insensitive to light hydrogen atoms in the presence of heavy cations such as Ba and Nb, it was not possible to crystallographically confirm the presence of the protons using these data.

To confirm the presence of an ordered proton position, the proposed structure of γ−III-$Ba_4Nb_2O_9 \cdot 1/3H_2O$ was Rietveld-refined against NPD data. Room temperature data collected on Echidna at $\lambda = 1.621$ Å were used for this purpose. Initial refinements were promising, with the introduction and refinement of the ordered proton resulting in improved refinement statistics. However, the Rietveld-refined structure still contained unacceptably irregular Nb_2O_9 and NbO_4 polyhedra, due to modulations in the $4 \times 2 \times 4$ supercell which our refinement of the subcell was not taking into account. In order to address this problem, and in an attempt to solve the superstructure, we carried out ab initio (DFT) geometry optimization calculations on a $4 \times 2 \times 4$ supercell of the

(26) Petricek, V.; Dusek, M.; Palatinus, L. *Jana2000. The crystallographic computing system*; Institute of Physics: Praha, Czech Republic, 2004.

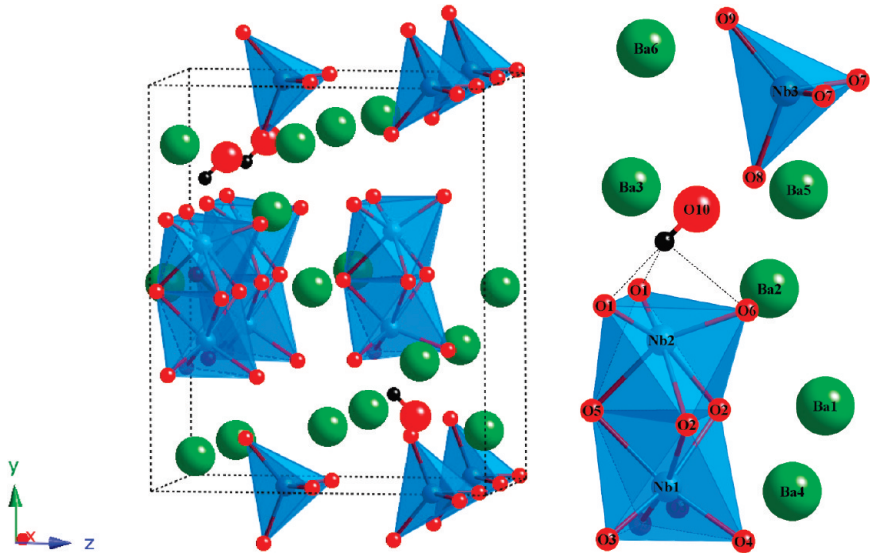

Figure 8. Structure of the orthorhombic subcell of γ-III-$Ba_4Nb_2O_9 \cdot 1/3H_2O$ at room temperature, from DFT geometry optimization and Rietveld refinement against NPD data. Ba atoms are green spheres; Nb_2O_9 dimers and NbO_4 tetrahedra are blue polyhedra with Nb atoms as blue spheres and O atoms are red spheres; OH groups are drawn explicitly with H atoms as black spheres. A representative part of the structure is expanded to indicate site labels and hydrogen bonds (dashed lines).

Rietveld-refined structure (which we distorted to monoclinic, $\beta = 90.3°$, based on S-XRD evidence). The energy of the structure converged monotonically to a robust minimum, at which point it contained highly regular Nb_2O_9 and NbO_4 polyhedra, and isolated OH groups that were clearly hydrogen-bonded to the three oxygen atoms on the exposed faces of Nb_2O_9 dimers. We found that the optimized superstructure could be collapsed back onto the $Pmn2_1$ subcell with atomic displacements no greater than 0.1 Å. Consequently, although no conclusions could be drawn from this result regarding the nature of the superstructure, it provided further support for our proposed average structure.

We then used the DFT-optimized model as a starting point for Rietveld refinement against NPD (Echidna) data. Instrumental and unit-cell parameters were refined initially, followed by isotropic atomic displacement parameters (ADPs) (constrained to be equal for atoms in chemically similar environments, and for atoms in the OH unit), resulting in a satisfactory fit to experimental data. The positions of Ba atoms (the most loosely bonded and therefore the least well-determined by DFT) and OH groups (the most interesting part of the structure) were then Rietveld-refined while Nb−O polyhedra remained fixed. The refinement converged readily with minimal atomic displacements. Most significantly, the unconstrained refinement of atoms in the OH groups resulted in chemically plausible O−H bond lengths of 0.95(15) Å, and H···O hydrogen bonds to the exposed faces of Nb_2O_9 dimers of 2.08(8) Å (× 2) and 2.18(8) Å. Several strategies were explored in an attempt to reduce the very large ADPs on the O atoms of the NbO_4 tetrahedron, and on the atoms of the OH unit, but without success. In particular, refining the positions of the O atoms in the tetrahedra (O7−9) and removing the constraint tying their ADPs together resulted in all three ADPs remaining very high. The only approach

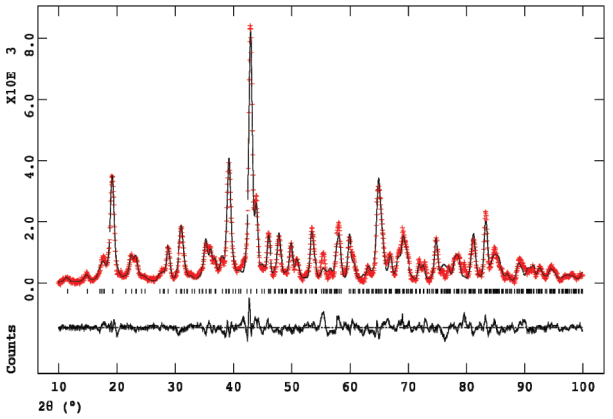

Figure 9. Observed (crosses), calculated (solid line), and difference (below) NPD (Echidna, λ = 1.621 Å) profiles for the final constrained Rietveld-refinement of the orthorhombic subcell of γ-III-$Ba_4Nb_2O_9 \cdot 1/3H_2O$ at room temperature.

that led to significantly reduced ADPs on these sites was to refine their fractional occupancies; however, the resulting fractional occupancies of ~0.35 on all three sites corresponded to a chemically unreasonable composition. These large ADPs on NbO_4 and OH units therefore suggest that these are the most strongly modulated in the 4 × 2 × 4 supercell; although they may also indicate local disorder within the 2D layers containing these structural elements. This question is discussed in subsection 5 below, in the context of our ionic conductivity results.

The final structural model for the subcell of γ-III-$Ba_4Nb_2O_9.1/3H_2O$, resulting from the combination of DFT geometry optimization and Rietveld refinement against NPD data, is shown in Figure 8. The final Rietveld-refined fit is shown in Figure 9, with refinement data and structural details summarized in Table 2. Full structural details including bond lengths are included in the deposited CIF file.

Table 2. Structural Details for the Subcell of γ-III-$Ba_4Nb_2O_9 \cdot 1/3H_2O$ at Room Temperature, From a Combination of DFT Geometry Optimization and Rietveld Refinement Against NPD Data (Echidna, λ = 1.621 Å)[a]

atom	*x* (*a*)	*y* (*b*)	*z* (*c*)	$100U_{iso}$ (Å^3)
Ba1	1/2	0.492(2)	0.984(3)	2.9(3)[1]
Ba2	1/2	0.6718(19)	0.304(3)	2.9(3)[1]
Ba3	1/2	0.8346(19)	0.029(3)	2.9(3)[1]
Ba4	1/2	0.3407(17)	0.346(3)	2.9(3)[1]
Ba5	0	0.862(2)	0.435(2)	2.9(3)[1]
Ba6	1/2	0.9113(17)	0.632(2)	2.9(3)[1]
Nb1	1/2	0.62836*	0.66558*	1.5(2)[2]
Nb2	1/2	0.38858*	0.65764*	1.5(2)[2]
Nb3	0	0.00458*	0.83953*	3.0(4)
O1	0.74376*	0.32029*	0.57899*	4.78(16)[3]
O2	0.72704*	0.51343*	0.73934*	4.78(16)[3]
O3	0.73299*	0.70315*	0.57846*	4.78(16)[3]
O4	1/2	0.71554*	0.81864*	4.78(16)[3]
O5	1/2	0.50600*	0.51681*	4.78(16)[3]
O6	1/2	0.33713*	0.82945*	4.78(16)[3]
O7	0.24174*	0.99765*	0.94989*	22.7(12)[4]
O8	1/2	0.85422*	0.27497*	22.7(12)[4]
O9	0	0.88741*	0.72263*	22.7(12)[4]
O10	0	0.827(7)	0.230(6)	29(4)[5]
H1	0	0.773(10)	0.166(17)	29(4)[5]

[a] Space group orthorhombic $Pmn2_1$ (No. 31); a = 6.0327(15) Å, b = 12.406(3) Å, c = 10.431(3) Å. GOF = 8.01 for 52 refined parameters. Overall powder R factors: R_p = 0.0505, wR_p = 0.0651, $R(F^2)$ = 8.47. Asterisks (*) indicate variables fixed to DFT-optimized values. Superscript symbols indicate constraints.

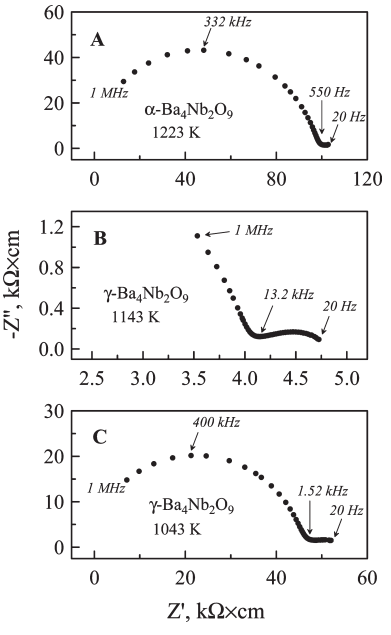

Figure 10. Impedance spectra of $Ba_4Nb_2O_9$ ceramics with porous Pt electrodes in air at $p(H_2O) \approx 50$ Pa.

4. Transport Properties. Figure 10 displays typical impedance spectra collected for the γ- and α-$Ba_4Nb_2O_9$ ceramics with porous Pt electrodes. The spectra consisted of two or three signals corresponding to the grain bulk, boundary, and electrode; regardless of the grain-boundary phenomena that become significant at temperatures below 1000−1200 K, the intercept of the high-frequency arc on the real axis makes it possible to calculate bulk (ionic + electronic) conductivity presented below. Notice that in all cases, this arc can be adequately described by a simple resistance-capacitance (RC) element, with no significant deviation from the origin at elevated frequencies. In the high-temperature range, the values of bulk conductivity calculated from the impedance spectra were found equal to the total conductivity measured by 4-probe DC technique, with an accuracy of 2%.

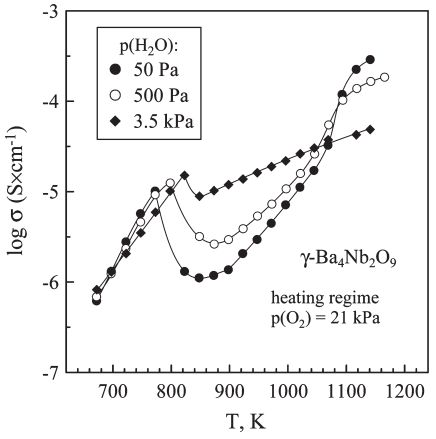

Figure 11. Total bulk conductivity of as-prepared γ-III-$Ba_4Nb_2O_9 \cdot 1/3H_2O$, measured on heating in flowing air at different water vapor pressures.

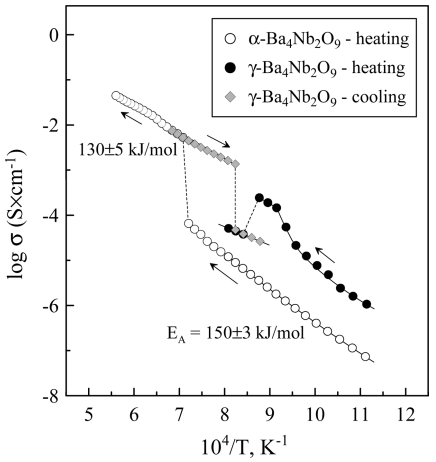

Figure 12. Total conductivity of as-prepared α- and -III-$Ba_4Nb_2O_9$, measured at $p(H_2O) \approx 500$ Pa and $p(O_2) = 21$ kPa, illustrating the $\alpha \leftrightarrow \gamma$ transition. The characteristic values of activation energy (E_A) calculated by the standard Arrhenius model are given in the legends. The arrows indicate direction of the temperature changes.

Figure 11 shows total conductivity variations on heating γ-III-$Ba_4Nb_2O_9 \cdot 1/3H_2O$ under different humidity conditions. The Arrhenius curves of α- and γ-$Ba_4Nb_2O_9$ on heating and cooling over a wide temperature range are compared in Figure 12. Several distinct temperature regimes related to the phase transformations are apparent. First, while the conductivity of γ-III-$Ba_4Nb_2O_9 \cdot 1/3H_2O$ increases with temperature, the dehydration and transition into γ-II-$Ba_4Nb_2O_9 \cdot 1/6H_2O$ leads to an abrupt decrease over the range 760−850 K (cf. Figures 4 and 11). As expected, increasing $p(H_2O)$ in the gaseous phase expands the stability domains of both hydrated polymorphs, γ-II and γ-III, shifting their decomposition to higher temperatures. The conductivity of γ-II-$Ba_4Nb_2O_9.1/6H_2O$ also increases with increasing the water vapor partial pressure. These trends

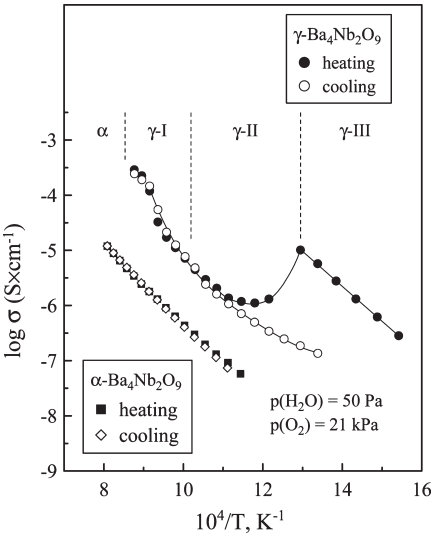

Figure 13. Total conductivity variations on heating and subsequent cooling in dry air ($p(H_2O)$ = 50 Pa) below the $\alpha \leftrightarrow \gamma$ transitions. The vertical dashed lines show approximate boundaries corresponding to the phase transformations in γ-$Ba_4Nb_2O_9$.

unambiguously indicate that, below 800 K when the water content in γ-III-$Ba_4Nb_2O_9$ is essentially stable (Figure 4), the conduction is substantially contributed to—or even dominated by—protons. A similar conclusion can be drawn from the hysteresis observed because of dehydration on temperature cycling in dry atmosphere (Figure 13). For γ-II-$Ba_4Nb_2O_9 \cdot 1/6H_2O$, the protonic contribution remains significant but non-negligible contributions of other charge carriers (oxide anions and electron holes) might be expected when $p(H_2O)$ decreases. These charge carriers become dominating for γ-I-$Ba_4Nb_2O_9$ formed on further heating and dehydration. This disordered phase exhibits a considerably higher total conductivity, which increases with decreasing $p(H_2O)$; as shown below, decreasing $p(O_2)$ leads to an opposite effect. Although the p-type electronic conduction is unusual for niobia,[27] hole transport is often observed in complex niobate compounds under oxidizing conditions.[5]

The transition of thermodynamically metastable γ-I-$Ba_4Nb_2O_9$ into the stable α polymorph is accompanied, again, by a conductivity decrease (Figure 12). (Note that the α phase formed in situ during conductivity measurements on heating and cooling the γ phase shows slightly higher conductivity than the annealed α sample; this may be explained by changes in the microstructure of the annealed pellets at the reconstructive phase transitions.) The transport properties of α-$Ba_4Nb_2O_9$ are substantially worse compared to γ-$Ba_4Nb_2O_9$ in the entire temperature range where the former modification exists, in agreement with our structural models. In combination with the lower proton concentration (Figure 4) and less pronounced hysteresis phenomena on temperature cycling (Figure 13), these results may suggest that the transport processes in α-$Ba_4Nb_2O_9$ under dry conditions are substantially contributed to by electronic charge carriers.

(27) Kofstad, P., *Nonstoichiometry, Diffusion and Electrical Conductivity in Binary Metal Oxides*; Wiley-Interscience: New York, 1972.

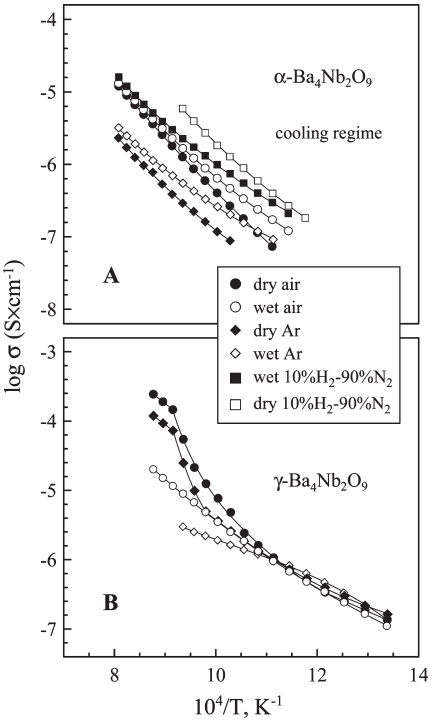

Figure 14. Total conductivity of $Ba_4Nb_2O_9$ ceramics, measured on cooling in atmospheres with different oxygen partial pressures.

In wet atmospheres, the protonic transport in α-$Ba_4Nb_2O_9$ becomes significant when temperature decreases below 1000 K, as indicated by increasing conductivity (Figure 14A). Another important feature revealed by the conductivity vs $p(O_2)$ dependencies of α-$Ba_4Nb_2O_9$ relates to the conductivity minimum in inert atmospheres. Such a behavior is well-known for proton-conducting oxides, such as acceptor-doped $BaCeO_{3-\delta}$ and $SrCeO_{3-\delta}$, where the total conductivity increases in both oxidizing and reducing environments due to rising p- and n-type electronic contributions, respectively.[2,18] Therefore, the conductivity of α-$Ba_4Nb_2O_9$ in air occurs most likely due to migration of protons, oxide anions and holes; whereas at low $p(O_2)$, protonic and *n*-type electronic contributions are expected to dominate. This conclusion is supported by the EMF data presented below. On the contrary, protonic conduction seems to prevail for the partly hydrated γ-II-$Ba_4Nb_2O_9$ in the intermediate temperature range, being essentially independent of the oxygen partial pressure (Figure 14B). Above the transition to γ-I-$Ba_4Nb_2O_9$, which has a very small water content (Figure 4), the conductivity variations are indicative of mixed oxide-ionic and p-type electronic conduction, as for $SrCe(Y)O_{3-\delta}$.[18]

Figure 15 shows ion transference numbers for α-$Ba_4Nb_2O_9$ ceramics under oxidizing conditions, determined by the EMF method, and Figure 16 shows the estimated ionic and electronic conductivities in dry and wet air, as calculated from the EMF and total conductivity data. These transport numbers are averaged under the given gradients of water vapor and oxygen partial pressures, and correspond to the ratio of ionic and total conductivities, i.e., $(\sigma_O + \sigma_H)/\sigma$, where σ_O and σ_H are

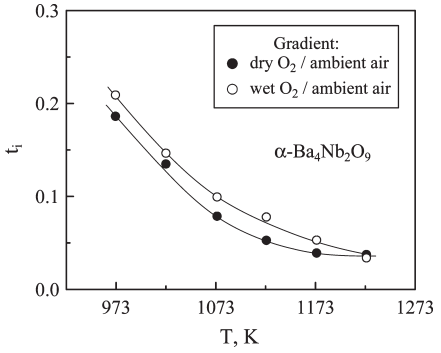

Figure 15. Ion transference numbers for α-$Ba_4Nb_2O_9$ ceramics under oxidizing conditions, determined by EMF method.

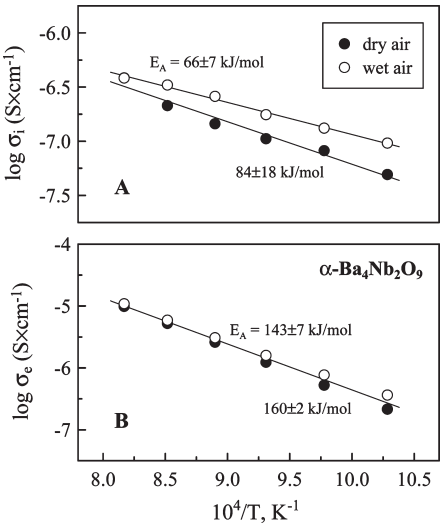

Figure 16. Estimated ionic ($\sigma_O + \sigma_H$) and electronic conductivities of α-$Ba_4Nb_2O_9$ in dry and wet air, as calculated from total conductivity and EMF data. Activation energies are given in the legends.

the partial oxide-ionic and protonic conductivities, respectively. The results confirm that the ionic contribution to the conductivity is relatively low (<25%) and decreases as temperature increases. This results from to the relatively low concentration of protons in the α phase, especially at elevated temperatures (see Figure 4), and because of the structural constraints hampering oxide ionic transport in this polymorph. The apparent activation energies for the overall ionic transport, occurring because of proton and oxide-ion migration, are 66−84 kJ/mol. This level of the activation energy is typical for many niobate phases,[4−6] and for numerous oxide-ionic conductors where the conductivity occurs via the vacancy mechanism.[27] The decrease in the E_A values in humid atmospheres is caused by increasing protonic conduction with a relatively low migration energy. The hole conduction activation energy is substantially higher, 143−160 kJ/mol.

5. Phase Diagram and Structure−Property Relations. The relationships among the different structural forms of $Ba_4Nb_2O_9$ with respect to temperature are summarized in Figure 17, based on the results of variable-temperature DTA, TGA, S-XRD, NPD, and dilatometry experiments. Note that hydration/dehydration steps are not abrupt, as they take place on a much slower time scale

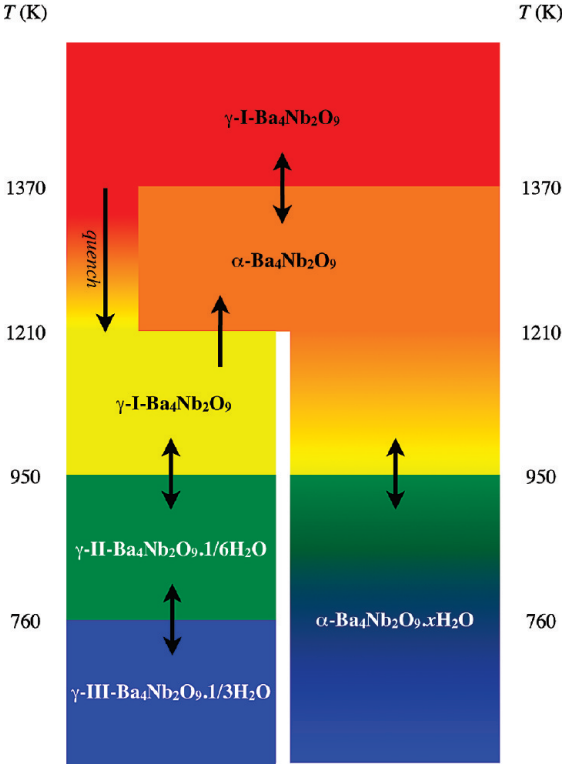

Figure 17. Phase diagram of $Ba_4Nb_2O_9$ consistent with the results of variable-temperature DTA, TGA, S-XRD, NPD, and dilatometry experiments.

than the structural transitions indicated. $Ba_4Nb_2O_9$ has two basic polymorphs: the high-temperature γ phase, which represents an entirely new structure type; and the low-temperature α phase, which is of the rare $Sr_4Ru_2O_9$ structure type. The phases are separated by a reconstructive phase transition at ~1370 K, the kinetics of which are sufficiently slow that the γ phase can easily be quenched to room temperature. Below ~950 K, both α and γ phases absorb significant amounts of water. Hydration, and accompanying proton and oxide ion conduction, is not unprecedented in Ba- and Nb-containing oxides, particularly BCN18 ($Ba_3Ca_{1+x}Nb_{2-x}O_{9-3x/2}$, $x = 0.18$) and $LaNbO_4$ which show proton conductivities up to 10^{-3} S cm^{-1} in wet atmospheres at 1100 K, compared to 1×10^{-4} S cm^{-1} under the same conditions in γ-$Ba_4Nb_2O_9$. However, some aspects of hydration in γ-$Ba_4Nb_2O_9$ are unusual. In particular, it appears that the presence of water stabilizes the quenched γ phase (which is the better ionic conductor) relative to the thermodynamic low-temperature α phase−i.e., it is actively stabilized by wet atmospheres, a desirable feature for potential applications. Only once dehydration is complete does it transform to the α phase, despite the existence at lower temperatures of hydrated versions of both phases with similar water content. It is interesting to note in this context that the cubic perovskite-type phase of $Ba_4Nb_2O_9$ reported by Wu et al.[16] was synthesized under extremely basic (i.e., proton-poor) conditions.

The improved stability of the quenched γ phase in wet atmospheres provides qualitative support for our crystallographic result that protons occupy ordered positions in

the structure. Hydration therefore gives rise to a stoichiometric phase γ-III-$Ba_4Nb_2O_9.1/3H_2O$ at room temperature. It is important to emphasize that we have not found exact structural solutions for this phase—single-crystal X-ray and neutron diffraction data clearly show that the structure we present here is only a subcell of a well-ordered monoclinic (or possibly triclinic) $4 \times 2 \times 4$ supercell containing several hundred crystallographically independent atoms. Finding an exact solution to this supercell is a significant long-term challenge on which we are still working with a modulated structure approach. Nevertheless, the results of careful DFT geometry optimization and refinement against single-crystal X-ray and NPD data, combined with TGA evidence for a stoichiometric hydrated phase and crystal-chemical considerations (notably the fact that Rietveld-refinement of OH groups produced plausible O—H covalent and O···H hydrogen bond lengths), gives us confidence that the average structure described here is correct.

γ-III-$Ba_4Nb_2O_9.1/3H_2O$ partially dehydrates on heating to give another stoichiometric phase γ-II-$Ba_4Nb_2O_9.1/6H_2O$, which on further heating completely dehydrates to γ-I-$Ba_4Nb_2O_9$. Both the γ-II and γ-I phases show modulation peaks in S-XRD data that are related to, but distinct from, those observed for γ-III. Further modulation peaks are observed at the transitions, suggestive of intermediate phases; however, this could also be explained by the fact that on warming, the structural phase transitions take place first and the dehydration follows on a slower time scale (comparing S-XRD and TGA data). The local structures of the γ-II and γ-I phases can be hypothesized at this stage. Clearly, complete dehydration results in the loss of all protons participating in OH groups, as well as half of the O atoms involved in those groups; and it is reasonable to assume that the remaining O atoms coordinate to Nb3 to form NbO_5 trigonal bipyramids. γ—II-$Ba_4Nb_2O_9 \cdot 1/6H_2O$ would therefore contain $3 \times NbO_4$ tetrahedra to $1 \times NbO_5$ trigonal bipyramids (and 1 OH group), whereas γ-I-$Ba_4Nb_2O_9$ would contain $1 \times NbO_4$ tetrahedra to $1 \times NbO_5$ trigonal bipyramid. However, the exact structures (and superstructures) of these phases will be extremely difficult to solve crystallographically.

If discrete, ordered OH groups are indeed present in the γ-III and γ-II phases, this would imply quite different ionic conduction mechanisms to those found in perovskite-type oxides such as BCN18. Hydration of such perovskites arises when pre-existing oxygen vacancies in the continuous network of corner-connected $(Ca,Nb)O_6$ octahedra are filled by OH^- anions, while the remaining proton from the hydrolyzed H_2O molecule bonds to a different O atom. Conductivity then occurs via intra- and interoctahedra proton transfer.[28] The maximum possible water content of BCN18 ($Ba_3Ca_{1.18}Nb_{1.82}O_{8.73} \cdot xH_2O$) is thus $x = 0.27$, although in practice the maximum observed is $x \approx 0.20$, with protons preferentially associated with the mixed Ca/Nb sites.[29] The situation in $Ba_4Nb_2O_9$ is different, as neither the α nor the γ phases contain continuously connected networks of octahedra. In α-$Ba_4Nb_2O_9 \cdot xH_2O$ (where we find no evidence for ordered hydration), if protons are closely associated with the vertices of NbO_6 octahedra, the fact that those octahedra form isolated Nb_2O_9 dimers rather than continuous corner-connected networks would explain the much lower proton conductivity compared to BCN18. However, in γ-$Ba_4Nb_2O_9 \cdot xH_2O$, in addition to layers of isolated Nb_2O_9 dimers we find 2D layers containing discrete OH groups and NbO_4 tetrahedra, both with very large ADPs. Although these large ADPs must be partly due to the structural modulation, they may also be indicative of extreme local flexibility in this part of the structure. It certainly seems likely that the much higher ionic conductivity of the gamma phases is due to these unique 2D layers. One could propose a simplistic mechanism in which the O atom of an OH group moves toward an NbO_4 tetrahedron and forms a strong bond, releasing the proton and resulting in an NbO_5 trigonal bipyramid and a free proton; in a concerted manner this would result in both proton and oxide ionic conduction. Molecular dynamics simulations and inelastic neutron scattering experiments are planned to explore the real mechanism.

Conclusions

Low-temperature α-$Ba_4Nb_2O_9$ has the rare $Sr_4Ru_2O_9$ structure type, while high-temperature γ-$Ba_4Nb_2O_9$ (found above ~1370 K) has a new structure type built of well-ordered layers of Nb_2O_9 face-sharing octahedral dimers, and flexible layers of NbO_4 tetrahedra and NbO_5 trigonal bipyramids. γ-$Ba_4Nb_2O_9$ is easily quenched to room temperature.

Both α and γ phases absorb significant amounts of water below ~950 K. In γ-$Ba_4Nb_2O_9$, protons occupy ordered positions, giving rise to a stoichiometric phase γ-III-$Ba_4Nb_2O_9 \cdot 1/3H_2O$ at room temperature. γ-III-$Ba_4Nb_2O_9 \cdot 1/3H_2O$ partially dehydrates at ~760 K to γ-II-$Ba_4Nb_2O_9.1/6H_2O$, which completely dehydrates at ~950 K to γ-I-$Ba_4Nb_2O_9$. All three γ phases have large, well-ordered superstructures that have not been solved, and which pose significant crystallographic challenges on which work is continuing.

Both phases show mixed proton, oxide ionic, and electronic conduction. Proton conduction dominates in the hydrated phases, with oxide ionic and electronic conduction playing increasingly important roles on dehydration. The hydrated γ phases exhibit faster protonic and oxide ionic transport than the hydrated α phases, because of the presence in the gamma phases of 2D layers containing Nb^{5+} cations with unusually low oxygen coordination numbers (4 or 5) separated by discrete OH groups. In addition to facilitating ionic conductivity, these OH groups appear to play an important role in stabilizing the γ phases at low temperatures, to the extent

(28) Kreuer, K. D. *Solid State Ionics* **1999**, *125*(1—4), 285–302.
(29) Shimoyama, T.; Tojo, T.; Kawaji, H.; Atake, T.; Igawa, N.; Ishii, Y. *Solid State Ionics* **2008**, *179*(7—8), 231–235.

that the $\gamma \rightarrow \alpha$ transition on reheating a quenched sample occurs at higher temperatures in humid atmospheres.

Acknowledgment. This work was supported by the Australian Research Council−Discovery Projects (DP0666465), the Australian Institute of Nuclear Science and Engineering (AINSE) Postgraduate Research Awards scheme, the FCT, Portugal (Project PTDC/CTM/64357/2006), and the NSF, USA (Project DMR-0502765). Travel to the FRM-II research reactor for NPD data collection was supported by AINSE.

Supporting Information Available: Crystallographic information files for α-$Ba_4Nb_2O_9$, Rietveld-refined against NPD data at 1273 K γ-III-$Ba_4Nb_2O_9$, optimized by DFT and partially Rietveld-refined against NPD data at 298 K. This material is available free of charge via the Internet at http://pubs.acs.org.